Radial Photonic Crystal for detection of frequency and position of radiation sources

J. Carbonell[1], A. Díaz-Rubio[1], D. Torrent[1], F. Cervera[1], M. A. Kirleis[2], A. Piqué[2] & J. Sánchez-Dehesa[1]

[1]Wave Phenomena Group, Universitat Politècnica de València, Camino de vera s.n. (Edificio 7F), ES–46022, Valencia, Spain, [2]Naval Research Laboratory, Code 6364 4555 Overlook Ave. S.W., DC 20375-5345, Washington, USA.

Based on the concepts of artificially microstructured materials, i.e. metamaterials, we present here the first practical realization of a radial wave crystal. This type of device was introduced as a theoretical proposal in the field of acoustics, and can be briefly defined as a structured medium with radial symmetry, where the constitutive parameters are invariant under radial geometrical translations. Our practical demonstration is realized in the electromagnetic microwave spectrum, because of the equivalence between the wave problems in both fields. A device has been designed, fabricated and experimentally characterized. It is able to perform beam shaping of punctual wave sources, and also to sense position and frequency of external radiators. Owing to the flexibility offered by the design concept, other possible applications are discussed.

M anipulation of light and its propagation characteristics has been a recurrent problem in the scientific community. Recent studies have made use of the so-called metamaterials to modify the propagation characteristics of electromagnetic waves almost at will, at least from a theoretical point of view[1,2]. These are artificially made microstructures, based on unitary elements of size much smaller than the wavelength of the illuminating radiation. The possibility of designing 'materials' with precise and controllable constituent parameters, those that define the solution of the wave propagation equations, has opened a very wide range of possibilities going from negative refraction[3], to sub-wavelength focusing[4] or cloaking[5]. A number of proposals exploit the exotic propagation characteristics that can be achieved by the proper design of microstructured propagation media[6–11]. These concepts can also be extended, with few limitations, to different application fields if they share a fundamental wave nature[12]. In this context, the research area has become truly multidisciplinary and one can cite as an example the recently proposed Radial Wave Crystals (RWCs)[13,14]. These microstructured devices are based on the idea of achieving cylindrical structures designed in such a way that their constitutive parameters can verify the Bloch theorem. When this is verified, propagation of electromagnetic or acoustic waves can be described by means of a dispersion equation or a dispersion diagram due to the intrinsic radial periodicity of the microstructures. The fundamental goal of these structures is to have a precise control of the allowed and forbidden propagation modes at the different frequency bands, since the concept does not present any limitation of frequency scalability. In turn, this permits thinking about different types of applications such as resonating elements, beam-shaping shells for radiation sources, frequency or position detectors for electromagnetic wave signals or even elements to allow a wireless power transfer between them[15].

In this article, we present the first practical realization of a Radial Photonic Crystal (RPC), the electromagnetic version of the RWC. A 2D device is designed starting from the constitutive parameter functions that determine a certain dispersion band profile. This profile is verified in a finite size microstructure implementing a reduced version of the ideal configuration, which yields an almost identical behaviour to the full version microstructure. The Radial Photonic Crystal is simulated, fabricated and characterized in a measurement setup. Comparison of the obtained results is given and analyzed, specially taking into account potential applications. Also, from measured and simulated results a parameter extraction is performed in order to recover analytically the order of the resonant mode at the frequency of operation. To conclude, we consider various potential applications beyond the ones presented in this paper and explain the fundamental aspects of the simulation, fabrication and measurement procedures in the Methods section.

Results

Design of a radial photonic crystal. The Radial Photonic Crystal design is based on recent theoretical work[13] where it is demonstrated that multilayered structures with radially periodic anisotropic parameters yield propagation media that verify Bloch's theorem. Therefore, it is possible to describe wave propagation by means of a dispersion diagram, where the band structure can be tailored according to the required objectives. For example, it is possible to fix the propagation band of one of the modes of the structure completely within the forbidden band of another one, or to fix the cut-off frequency of a certain mode coincident with the beginning of the forbidden band of a lower order mode. To achieve these and other features, constitutive parameters have a radial dependence and are defined with tensors: they are anisotropic. We may chose working with TM waves to make a practical design, although equivalent designs and behaviours exist for TE waves and also for acoustic waves. If we take TM^z waves (z-polarized E-field) we have three parameters to define: $\mu_r(r)$, $\mu_\theta(r)$ and $\varepsilon_z(r)$. In view of making a practical device we have designed a multilayered structure (concentric pairs of alternating layers of types a and b). The microstructure has unitary cell parameters, respectively for layers a and b, given by the following equations:

$$\mu_{ra}(r) = \frac{d}{0.347r} \qquad \mu_{rb}(r) = \frac{d}{0.5r}, \qquad (1)$$

$$\mu_{\theta a}(r) = \frac{0.08r}{d} \qquad \mu_{\theta b}(r) = \frac{0.04r}{d}, \qquad (2)$$

$$\varepsilon_{za}(r) = \frac{d}{0.143r} \qquad \varepsilon_{zb}(r) = \frac{d}{0.1r}, \qquad (3)$$

where $d = d_a + d_b = 5 + 5$ mm is the radial periodicity (see Fig. S1 for a graphical representation). These functions generate a set of three anisotropic parameters that can be implemented by means of structured arrays of elements fabricated with standard patterning and etching techniques. This system may be scalable in frequency by varying periodicity parameter d, with only the obvious limitations related to any practical implementation. A radial multilayered
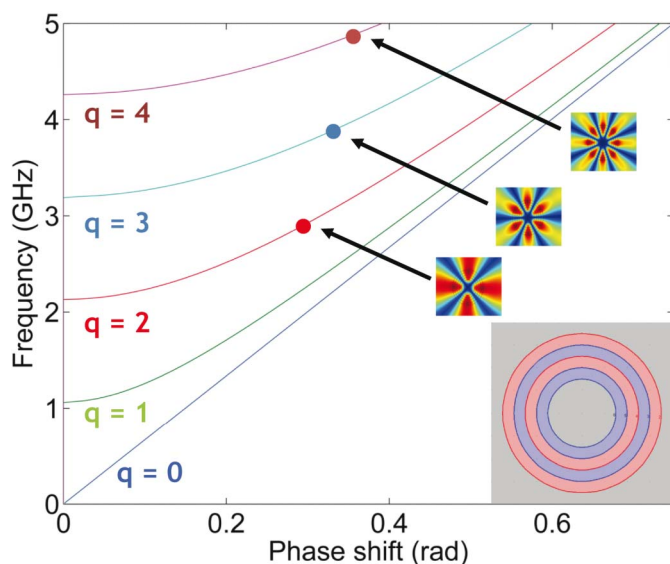

Figure 1 | Dispersion diagram of the ideal RPC structure with full set of constitutive parameters. Cut-off frequencies of modes with $q > 0$ are equally spaced (aprox. 1.1 GHz). Lower right inset represents a 4 layers (finite size) device with internal cavity of radius $r = 15$ mm and periodicity $d_a = d_b = 5$ mm. Dots and associated E-field patterns correspond to the resonance frequencies of the selected operation mode ($q = 3$; $f = 3.8$ GHz) and adjacent ones of the 4-layers RPC shell.

structure having these constituent parameters has the dispersion diagram shown in Fig. 1. The first 5 modes are represented corresponding to the unit cell analysis (infinite periodic structure). The inset at the lower right corner shows the scheme of a 4 layers structure (2 a-type layers and 2 b-type layers). This finite size structure has an internal cavity in order to assure that $\mu_r(r)$ and $\varepsilon_z(r)$ do not reach infinite values at the centre of the shell. Also, superimposed on the curves are some of the E-field patterns of the Fabry-Perot resonances corresponding to the finite size structure. The symmetry order of these modes can be easily identified since the number of lobes in the E-field patterns is double with respect to the resonance order. Only the first mode ($q = 0$) does not have a cut-off frequency, the rest have almost equally spaced cut-off frequencies (1.1 GHz difference). In what follows, the selected operation frequency corresponds to the $q = 3$ Fabry-Perot resonance of the four layers device ($f = 3.8$ GHz, corresponding to a vacuum wavelength $\lambda_0 \approx 79$ mm). Regarding the impedance and refractive index values, directly obtained from the permittivity and permeability, both have values close to the background (vacuum), thus assuring a reasonable match between the shell and the surrounding medium (see Fig. S2).

Although it should be possible to implement a device with the full set of parameters previously given, we simplified the structure to a reduced parameter set for the sake of fabrication time. The dominant parameter in terms of functionality is the angular permeability $\mu_\theta(r)$, therefore it is important to keep it unchanged. It is equivalent to ρ_r (the radial component of the inertial mass) in the acoustic counterpart of the device[13]. The other two parameters ($\mu_r(r)$ and $\varepsilon_z(r)$) are replaced by their *corrected* mean values (see supplementary materials). With these assumptions, a simple way to implement the permeability and permittivity functions is using arrays of Split Ring Resonators (SRRs)[16], with one metallic ring on each side of a dielectric substrate. Let us recall that SRRs arrays have a frequency dispersive Lorentz-type resonant magnetic response[17]. This response is generated by a magnetic field perpendicular to the rings plane. Depending on the geometry of the split rings, it is possible to obtain a wide range of potential permeability values at a specific frequency (since it is a resonant response giving values from negative to positive). A scheme of the proposed structure is displayed in Fig. 2(a). This structured resonator array has an anisotropic permeability tensor with mainly an angular magnetic response in the cylindrical coordinate system. Also, it has an electric response derived from the dielectric substrate between the metallic rings and the currents flowing through the rings. A similar type of structure has been employed specifically in a context of beam-shaping applications[18]. Our design is formed of 4 concentric arrays (layers) of SRRs having the unit cell parameters shown in Fig. 2(b). Exact values of each dimension are given in the supplementary materials. The geometric parameters that differentiate the concentric layers are the metallic pattern widths (w) and the ring gap (g). Each layer is therefore formed by an integer number of identical unit cells that synthesise the $\mu_\theta(r)$ values displayed in Fig. 2(c). The variable function of $\mu_\theta(r)$ has a stair-like profile. The continuous variation within each layer given by Eq. (2) is here replaced by stepped values of $\mu_\theta(r)$ since the periodicity parameter d is small enough compared to the operation wavelength to permit this discrete approximation. Let us note from Fig. 2(c) that $\mu_\theta(r)$ values are between 0 and 1, $\mu_r(r) = 1$ (no radial magnetic response) and $\varepsilon_z(r) = 3.4$ (constant with the radial coordinate). It is assumed that the fact that the SRRs are organized in concentric circular layers does not modify seriously the response obtained from the one of a square unit cell as the one used in Fig. 2(b). In this case, this approximation is better for the large radius or external layers.

One sample of the fabricated RPC shells is displayed in Fig. 3(a). It has an inner cavity with radius $r_{int} = 15$ mm and an external radius of $r_{ext} = 35$ mm. The diameter of the shell is smaller than one wavelength at the operation frequency. It includes a foam support
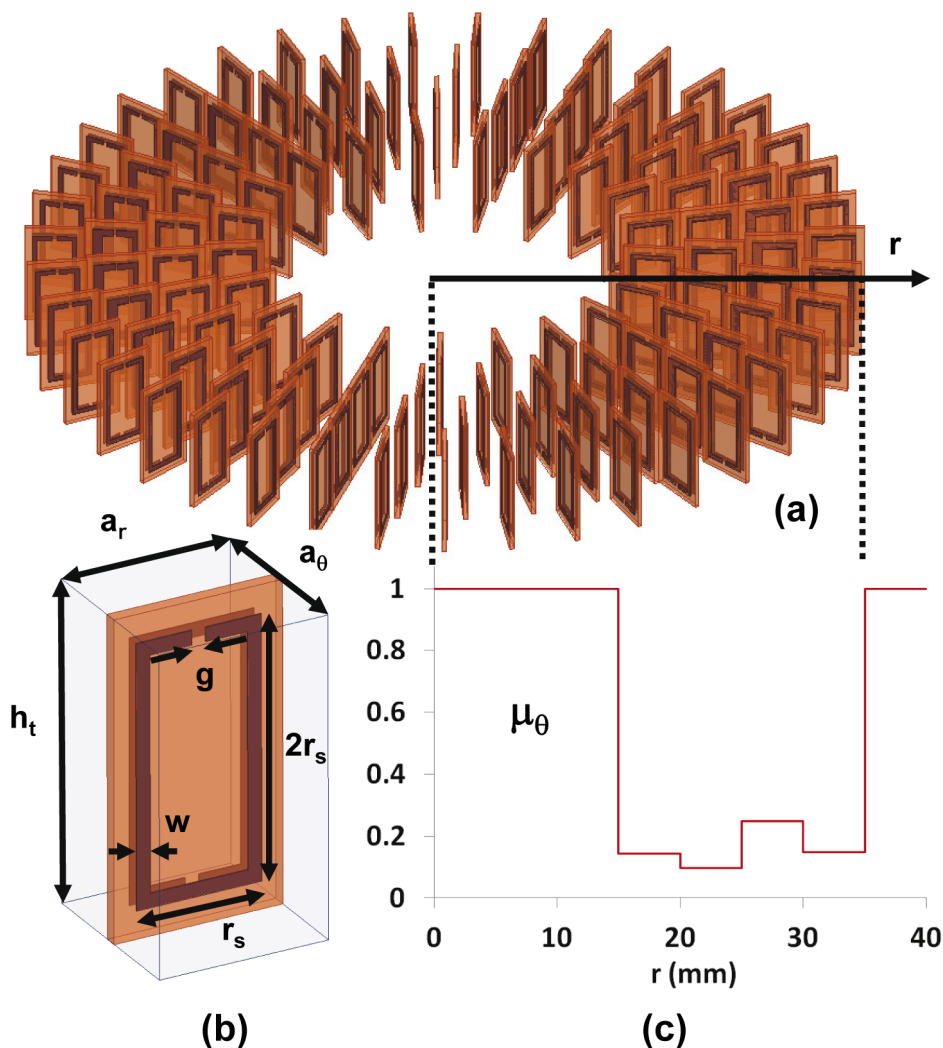
Figure 2 | (a) Implementation scheme of a 4 layers RPC; (b) unit cell characteristic dimensions and simulation domain for constitutive parameters extraction; (c) angular permeability profile as a function of the radial coordinate showing a stepped profile for the 4 layers device.

of Rohacell ($\varepsilon_r \approx 1$) to position and hold the SRR arrays. This support is neutral to the EM fields. The SRRs are made of metallic strips on both sides of dielectric substrate plates. The employed measurement setup (see Fig. 3(b)) is a parallel plate waveguide where the RPC is illuminated with punctual sources (within the inner cavity or externally) or alternatively with a plane wave. Field maps can be obtained with a Vector Network Analyzer by varying the position of a sensing probe and by recording the transmission and reflection coefficients. This is an automated procedure as explained in the Methods section that yields magnitude and phase information of the E-fields.

Characterization. In a first stage, the designed device has been first analyzed with a 2D finite element solver[19] by defining the shell directly using Equations (1) to (3). Then, constitutive parameters have been adapted (and reduced) for the different layers forming the device using the values given in Fig. 2(c). In both cases, we call this an analytical definition of the RPC. This permits the analysis of the multilayered structure in terms of an eigen-value problem to extract the Fabry-Perot resonance frequencies displayed in Fig. 1. Also, by including point (or line if considering the z-invariance) sources, it is possible to obtain field maps of the interaction source + shell. In a second stage, the geometry of the shell can be translated to the SRR arrays design. This is performed with a 3D finite element solver[20] that allows the optimization of the SRR dimensions to produce the target parameters of Fig. 2(c) through standard

retrieval techniques[21]. These are independent unit cell simulations (as from Fig. 2(b)) and the complete procedure for the four layers gives a full geometric definition of the RPC. Then, once the geometry of each layer is finalized, it is possible to perform numerical simulations of the four layer SRR shell (Fig. 2(a)) to obtain the field patterns at different frequencies and source positions. These are ab-initio simulations that yield the E-field patterns on the top plane of the simulation domain of Fig. 2(a), where also the sensing probe of the measurement setup captures the measured values. Finally, an extensive measurement process is performed for different configurations with two prototype devices. Therefore, we obtain three sets of comparable results: analytical simulations, ab-initio simulations and measurements.

Analysis of the first configuration consisted of a point source located within the inner cavity of the shell ($r = 11$ mm from its centre). This source radiates at a frequency corresponding to the $q = 3$ Fabry-Perot shell resonance ($f = 3.8$ GHz). Thus, Fig. 4 displays the E-field patterns of the combined shell + source structure, where the RPC acts as a beam-forming shell. Isotropic radiation of the point source is transformed onto a sextupole radiation pattern, corresponding to the mode order of the excited shell resonance. Obviously, this effect can apply to the rest of the resonant modes of the shell, at each frequency, with its corresponding beam shaped radiation pattern. To excite modes with symmetry $q > 0$, the inner source must be placed at a position displaced from the exact centre of
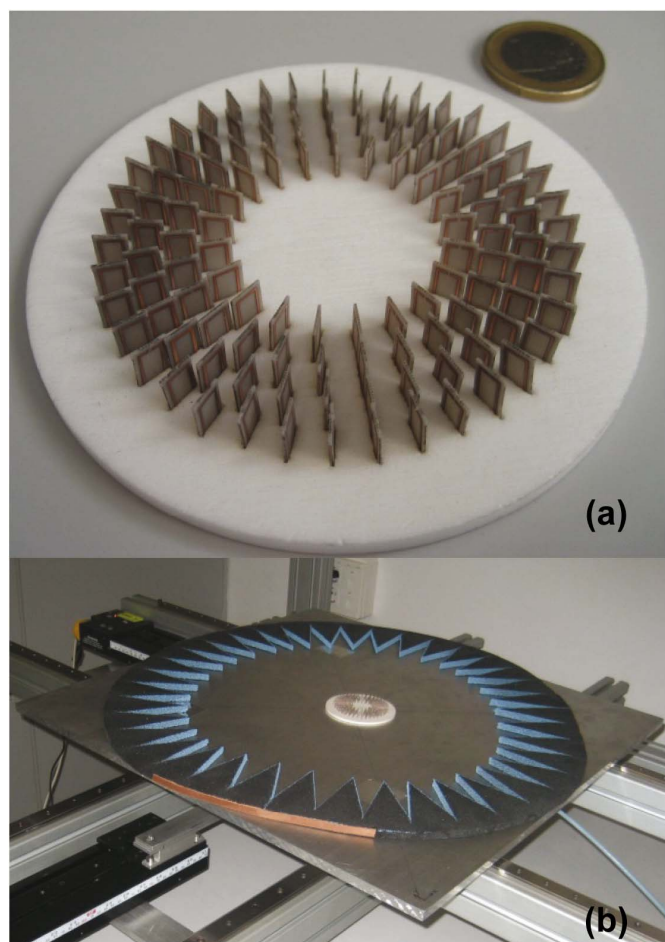
Figure 3 | (a) Radial Photonic Crystal shell including a Rohacell foam support for positioning and holding the SRR arrays; (b) measurement setup (top plate is removed to allow inner vision) including positioning system in two perpendicular axis.

the cavity. Similar field patterns can be observed on all three panels, with slight differences basically due to the discrete implementation scheme (this can be seen in panels b) for the ab-initio simulation and c) for the experiment). Furthermore, the experiment also shows that shell lobes close to the inner source have higher strength. Such an effect is more pronounced than in the ideal Comsol simulation. These results confirm that, on the one hand, the design procedure is validated through the SRR implementation. On the other hand, the functionality of the resonant shell is verified, since it can shape the radiation pattern of the point source.

A second alternative is to excite a RPC with an external point source at the resonance frequency of the shell. This means that depending on the frequency of the external source that illuminates the shell, a specific mode can be excited. An example of this is provided in Fig. 5, where results from analytical simulation, ab-initio simulation and measurement are displayed. The point source is located at a distance of 95 mm ($>\lambda_0$) from the centre of the shell and it radiates again at the nominal frequency $f = 3.8$ GHz. If the microstructure is designed to resonate at specific frequencies, it can detect the presence of radiators at these frequencies that would excite the corresponding shell resonances. The shell resonant pattern can therefore identify the radiation frequency of the external source (within a limited number of frequencies, see Video S1 in the supplementary materials). One additional interesting point of this scenario is the fact that the resonant pattern in the RPC shell has one of its lobes oriented towards the external source. In this example, it is the

one with the lowest intensity. This enables locating the position of the emitting source according to the resonant pattern orientation. This pattern can be especially accurate if several RPCs are used simultaneously at a $q = 1$ symmetry resonance (see Video S2 in the supplementary materials).

For example, if two identical shells are illuminated by the same source, then it is possible to use the pair of shells and their respective resonance patterns to identify the position of the emitting source. Such configuration is depicted in Fig. 5 where two identical shells are illuminated by a single point source located approximately at 90 mm from their centres. The real part of the E-field is displayed and consistent results are observed between all three field maps. The main application of this feature is for position detection of point sources by triangulation (see the supplementary materials for more details on the position determination). At last, a final measurement has been performed in order to test the utility of the proposed design in view of detecting plane waves (distant sources). In this case, a modified setup has been employed with a large parabolic type reflector located at the extreme left side of the measurement setup. Although imperfect, the reflector produces a plane wave to illuminate the RPC. Results are displayed in Fig. 7, where it can be noticed that the quasi-plane wave again excites the $q = 3$ resonant mode of the shell. The illuminating wave is slightly bended because the distance from the reflector to the shell is short and approximately equal to two wavelengths.

As a general comment to these comparisons between simulations and measurements, it is easy to observe how the response of first the ab-initio simulation (SRR design) and then the fabricated shell are progressively degraded with respect to the ideal 2D analytical simulation. Since ab-initio simulations and measurements are performed on a true 3D configuration, only the top plane of the microstructure can be mapped. This top plane includes the splits of the rings that locally concentrate high E-fields. Although for the 3D cases the obtained results clearly reproduce the expected 2D behaviour, this effect is superimposed to the shell resonance.

Extraction of resonant mode coefficients. One additional step in the analysis of the measured and simulated results is performed through the extraction of resonant mode coefficients from the measured or simulated field maps. These field maps represent a linear combination of the waves emitted by the source and the scattered response of the shell when these waves impinge on it. These responses can be evaluated, for cylindrical waves, from the summation of Bessel and Hankel functions of different orders (q values), with amplitude coefficients that depend on the strength of the respective contributing modes. This procedure allows evaluating what modes are present, or even dominant, at each frequency and it helps to define where the resonance frequencies are located. Starting from the configuration of Fig. 5, the measured area can be divided in two regions. First region (I) is the one outside of the shell, where the direct source contribution and scattered contribution from the shell are added. Second region (II) is the inner cavity of the shell where the field is only composed of the scattered response from the shell. Although this type of analysis can be carried out in both regions with the reported difference, we can express the field for the second region as:

$$\psi_{\mathrm{II}} = \sum_{q=-\infty}^{\infty} \mathrm{B_q} J_q(kr) e^{iq\theta}, \qquad (4)$$

where J_q are Bessel functions whose coefficients B_q are unknown. A linear regression fit is applied to obtain the B_q values from the field maps of the simulated and measured results. Results of this regression analysis are plotted in Fig. 8 for the modes $q = 1, 2, 3$. A high coefficient of determination ($R^2 = 0.9986$) is obtained from the regression analysis of the measured results, which is better than for the analysis of the region outside the shell (region I). It is clearly
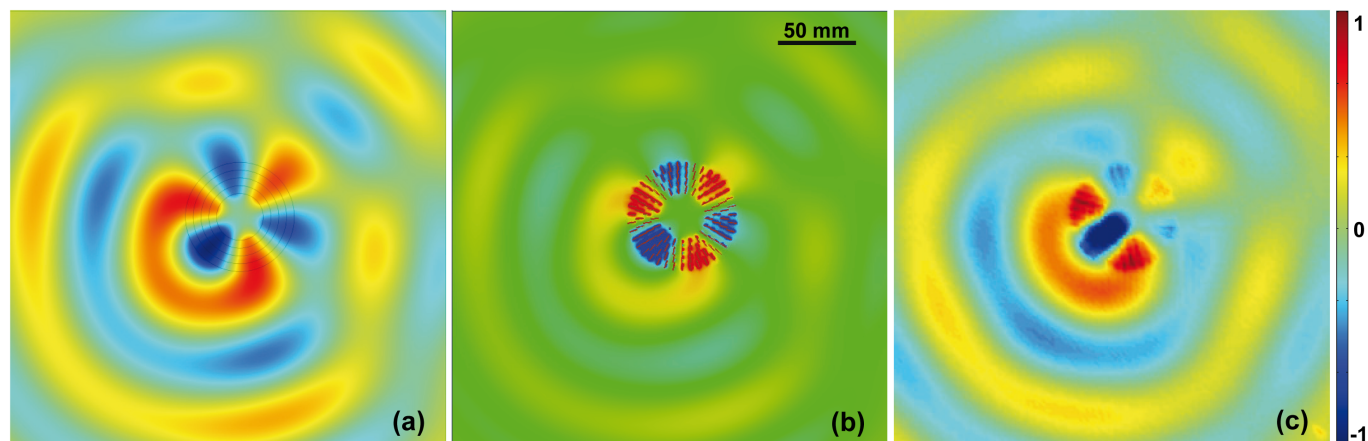
4

Figure 4 | Real part of the E-field map of a point source placed inside the RPC shell (in the inner cavity) and radiating at a frequency $f = 3.8$ GHz ($q = 3$ mode): (a) analytical simulation; (b) ab-initio simulation; (c) measurement results. Field scale is normalized with respect to the extreme values in each plot.

observed that in a wide frequency range close to the nominal resonant frequency the dominant mode has a symmetry order $q = 3$.

Discussion

Several points merit a specific discussion in the design of the proposed devices. The procedure followed with these microstructures is not based on transformation optics, as it is done usually for other complex metamaterial-inspired devices[22]. In our case, it is a design directly based on dispersion diagram engineering, with selection of the allowed and forbidden resonant modes. Essentially the structures behave as Fabry-Perot resonators, although inner cavity (Bragg) RPC resonances may also be used for creating very high quality factor (Q-factor) resonances, as it was demonstrated in acoustics[14]. The particular design selected in this case has, on the contrary, very low Q-factor resonances. This is mainly due to the fact that the devices are specifically adapted to the background. Therefore, impedance matching, achieved with reduced impedance values close to one, is a target for the microstructures. This fact has a twofold implication. On the one hand, it provides quite wide resonances (Q-values are close to 10 at the operation frequency). On the other hand, and since the resonance is not very sharp, the designed microstructure can work not only at the exact resonance frequency, but also over a wide range around this nominal value. This means that fabrication and measurement uncertainties can be accepted without excessive

degradation the operation features of the devices. From these characteristics, the proposed design is well suited for the applications described in this work, i.e. interaction with radiation sources. EM fields will interact intensely with the shells at and close to the resonance frequencies.

Another point is related to the slight but systematic difference we found between the resonance frequencies of the designed devices, and the measured ones. This refers to the fact that simulations in Fig. 3 to Fig. 7 are given at 3.8 GHz, whereas measured results are actually given at 4 GHz. From the discussion in the previous paragraph, we experimentally noted that, good results were obtained at 3.8 GHz (in terms of agreement with simulations), but the shells had better defined resonant patterns at 4 GHz. Although a number of factors can have an effect on this problem, we identified the one responsible for most of this deviation. Some of the factors can be attributed to fabrication tolerances in the geometrical dimensions, uncertainties in the exact value of the dielectric constant of the substrates employed for the SRRs, or imperfections in the design of the measurement setup. Systematically we have obtained slightly better results at frequencies slightly above the nominal 3.8 GHz frequency. This is in a large part due to the fact that our experimental setup is based on mobile parallel plates with the RPC in between them. With this scheme, it is not possible to exactly separate the two metallic plates a distance equal to the RPC shell height (h_t). Otherwise, the
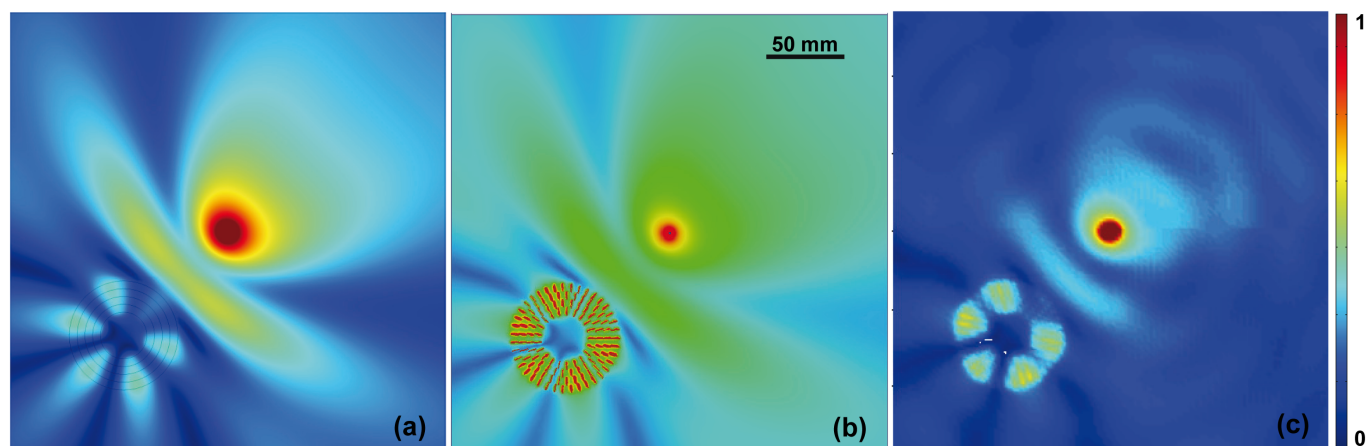

Figure 5 | E-field complex magnitude map for a point source illuminating the RPC shell (source – center separation $r = 95$ mm) and radiating at $f = 3.8$ GHz ($q = 3$ mode): (a) analytical simulation; (b) ab-initio simulation; (c) measurement results. Field scale is normalized with respect to the maximum value in each plot.
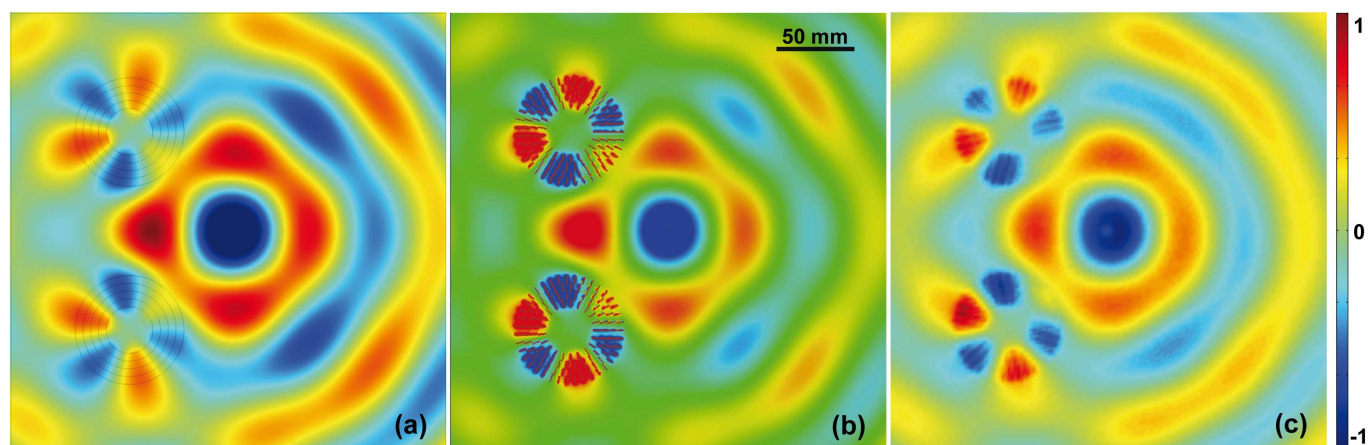
Figure 6 | Real part of the E-field for a point source illuminating 2 RPC shells at a distance of approximately 90 mm to their centres and radiating at a frequency f = 3.8 GHz (q = 3 mode): (a) analytical simulation; (b) ab-initio simulation; (c) measurement results. Field scale is normalized with respect to the extreme values in each plot.

relative movement between the plates could easily displace the shell and invalidate the measured field map. Let us note also that the probing antenna of the top metallic plate is designed to penetrate a minimum possible depth inside the inter-plate space. This trade-off guarantees a sufficient measured signal level but also a minimum invasion in the measured plane (and in principle no contact with the shell). In practice approximately a 1 mm air gap was left between the top of the shell and the upper metallic plate. This was the minimum safety separation to avoid mechanical displacement of the shell with the plate movement. Nevertheless, this air layer on top of the shell had an impact on the constitutive parameters theoretically synthesized with the SRR arrays. Actually, it modified them by basically increasing the permeability values and decreasing the permittivity values. The combined effect produced a slight increase of the resonant frequency, verified by simulating each unit cell (as in Fig. 2(b)) including the upper air gap. This explains why results are better at 4 GHz instead of 3.8 GHz, the nominal resonance frequency. Also, in Fig. 8, the maximum of the B_3 coefficient is obtained at around 4 GHz, although at 3.8 GHz the mode with q = 3 is still the dominant one. Simulation results in Fig. 8 do include the 1 mm air layer (additional simulation details are given in the Methods section).

Overall, the design flexibility offered by the proposed concept of Radial Photonic Crystal allows many different applications for these microstructures. At the opposite side of the considered constitutive

parameters, we may think of a configuration with very high values of permittivity and permeability (as high as it could be achieved from an implementation point of view). In this complementary scenario, very sharp resonances would be obtained with large E-field values confined within the resonant shells. This situation could be very well suited for wireless power transfer applications. In this case, it is intended to transfer power between identical resonators that are placed within a moderate separation (wireless transfer). The long evanescent fields (not radiated as in the reported configuration) may be used for this power transfer, since they would provide electromagnetic energy from one RPC acting as an active source (or feeder) and a second one acting as a receptor. The feeder would be configured with a point source within the inner cavity. For this type of application it is mandatory to use resonators with high Q values. This is possible by proper engineering of the constituent parameters so that impedance and refractive index allow the devices to highly confine the EM fields within the shell region. Energy transfer is then possible through the evanescent mode tails outside the shell of the resonance patterns by proximity coupling (strong coupling regime). However it is not always necessary that both coupled resonators be placed at a very short separation between them to make the wireless power transfer efficient[15].

In this work, we have demonstrated the feasibility of Radial Photonic Crystals, a class of metamaterial-based microstructures with a large number of potential applications. We experimentally
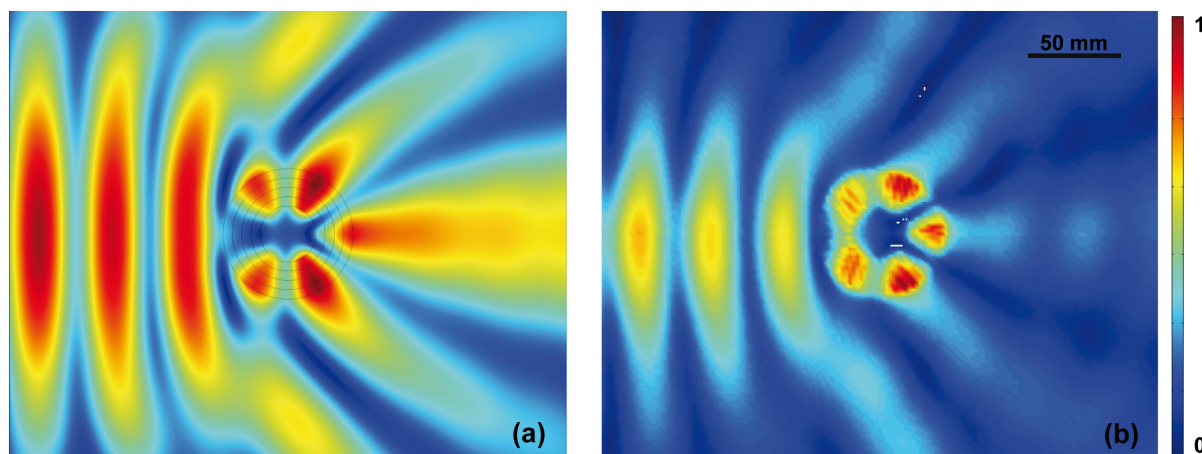

Figure 7 | E-field complex magnitude map for a plane wave illuminating an RPC shell at a frequency f = 3.8 GHz (q = 3 mode): (a) analytical simulation; (b) measured results. Results in (a) include a deformed (slightly bended) wave shape according to the practical setup characteristics. Field scale is normalized with respect to the maximum value in each plot.
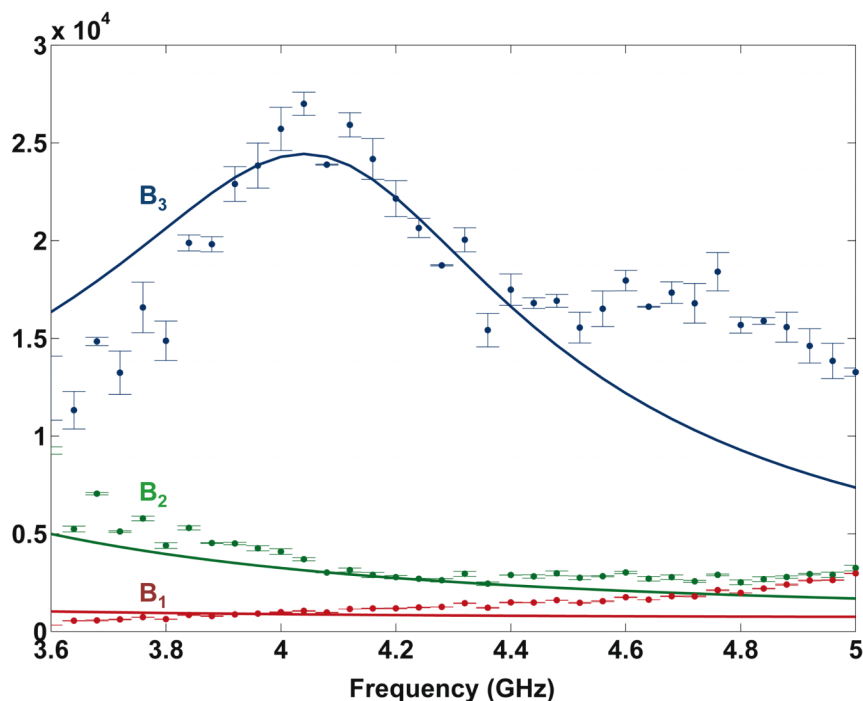
Figure 8 | Extracted coefficients from the inner cavity field values for the first 3 modes. Results from measurements are displayed with symbols and include 95% confidence intervals from the regression analysis as error bars; results extracted from analytical simulation are displayed with solid lines.

validated the theoretical concept through the design of a microwave shell that permits modifying the radiation characteristics of point sources and generating radiation diagrams based on the shell resonances. Also, these devices permit, by means of a proper design, identifying the radiation frequency and position of external point sources. An overall good agreement has been obtained between the designed shells and the measured results by comparing electric field maps in terms of magnitude and real parts. Moreover, the experimental data also confirm the resonance behaviour by means of an analytical extraction of the resonant mode coefficients, and clearly identify the resonating mode in the RPC shell. A broad spectrum of potential applications is now open for the use of these microstructures that are scalable with frequency and can be translated into the acoustic domain.

Methods

Device fabrication was performed either by standard techniques involving laser patterning of a spin-coated polymer layer and chemical etch of the exposed metal in a first run or a multistep process combining laser micromachining, protective layer definition and chemical etch in a second run. Although the second process guarantees an accurate and better definition of all geometrical dimensions, it turns out that the first process resulted in a globally better response for the fabricated RPC shell. We believe a certain degree of contamination of the composite substrate was generated during laser micromachining in the second process, thus degrading the resonant response. The substrate used for both processes was Neltec NY9220 with low permittivity and loss ($\varepsilon_r = 2.2$ and $tan\ \delta = 0.0009$), with uniform dielectric (0.381 mm) and metal (35 μm) thicknesses for all layers. This observation is in accordance with the first point of the Discussion section. Even if there were slight differences in the dimensions generated because the fabrication tolerances of the first process, the obtained results in terms of device operation were not affected in a sensible manner. On the contrary and as a result of the second fabrication process, metallic particles embedded in and contaminating the dielectric substrate did affect more the operation of the device.

The measurement setup consisted of a parallel metallic plate setup, with a mobile lower plate with respect to the fixed upper one. The movement between them is linear in two orthogonal axes. General details about this type of setup can be found in previous works[5,23,24]. Specific characteristics of our setup are described next. The total useful measurement area was approximately 280×280 mm², divided in 4 consecutively measured quadrants. The resolution employed was identical in both movement axes, 2 mm, since the sizes of the employed SMA connectors used as emitting and sensing probes were about 1 mm in diameter. We used a nominal separation between

both metallic plates of approximately 10 mm, taking into account that the shell height is $h_t = 9$ mm and approximately 1 mm gap is left above the shell to avoid contact with the upper plate sensing connector. In the case of the plane wave excitation, a connector combined with a 2D reflector of a parabolic type is employed as the radiation source. The setup allows retrieving information on relative magnitude and phase of the electric field.

The fact of using SRR arrays to implement the RPC shell implies that the dispersive behaviour of the SRR unit elements will interact with the expected behaviour of the shell as a whole, since constitutive parameters will not be constant with frequency[17]. This problem was alleviated by using constitutive parameters in a region where dispersion is limited for permeability and almost inexistent for permittivity (see Fig. S3 in the supplementary materials). Actually, the synthesized values of μ_θ are between 0 and 1, in a region of the Lorentz-type permeability curve where variation with frequency is very smooth. This allows limiting the impact of SRR dispersion on the operation of the RPC shell. Nevertheless, below 3.5 GHz it is expected that the SRR arrays generate negative values of permeability, while approaching the resonance frequency, therefore results below that frequency point completely disagree with the expected analytical (non-dispersive) RPC behaviour. On the contrary, above the operation frequency (3.8 GHz), and since the permeability variation is very smooth, the SRR dispersion influence in the RPC shell behaviour is very small and consistent results can be obtained from the fabricated shells, as showed in Fig. 8.

A linear regression analysis is used to obtain the extraction coefficients displayed in Fig. 8. This regression analysis is based on identifying the B_q coefficients in Equation (4) by fitting the measured and simulated field maps to this expression. This permits calculating a coefficient of determination R^2 giving the fraction of the field variation explained by the equation model. In our case, R^2 is very high for the measurements because we use the field map only inside the inner cavity. This limits the external sources of error that impact more on the field pattern external to the RPC. It is also possible, from the residual variance of the measured data, to calculate the 95% confidence intervals as plotted in Fig. 8. Confidence intervals for the simulated data are not included in this plot, since for the simulations R^2 is equal to 1 in practice.

Finally, the extracted coefficients in Fig. 8 are directly obtained from the measured field map by processing it. In the case of the ones derived from the analytical simulation, they require some additional explanation. Taking into account the slight resonance frequency shift generated by the air layer above the RPC, we performed a new series of simulations of the unit cells (as in Fig. 2(b)) but this time including an extra 1 mm air layer above the SRR. This generated a set of new constituent parameters at 3.8 GHz (the operation frequency). This variation is at the origin of the observed frequency shift. In order to check that this agreed with the experimental observation, we performed a new analytical simulation with the second set of constitutive parameters (those obtained at 3.8 GHz and invariant with frequency) to obtain a new field map for the RPC illuminated by the external source, as in the measurement. This time the analytical resonance frequency of the $q = 3$ mode is also shifted upwards and in practice matches the one obtained in the measurements, as it is confirmed in Fig. 8.

1. Pendry, J., Schurig, D. & Smith, D. Controlling electromagnetic fields. *Science* **312**, 1780–1782 (2006).
2. Leonhardt, U. Optical conformal mapping. *Science* **312**, 1777–1780 (2006).
3. Smith, D., Padilla, W., Vier, D., Nemat-Nasser, S. & Schultz, S. Composite medium with simultaneously negative permeability and permittivity. *Phys. Rev. Lett.* **84**, 4184–4187 (2000).
4. Pendry, J. B. Negative refraction makes a perfect lens. *Phys. Rev. Lett.* **85**, 3966–3969 (2000).
5. Schurig, D. *et al.* Metamaterial electromagnetic cloak at microwave frequencies. *Science* **314**, 977–980 (2006).
6. Narimanov, E. E. & Kildishev, A. V. Optical black hole: Broadband omnidirectional light absorber. *Appl. Phys. Lett.* **95**, 041106 (2009).
7. Grbic, A. & Eleftheriades, G. Overcoming the diffraction limit with a planar left-handed transmission-line lens. *Phys. Rev. Lett.* **92**, 117403 (2004).
8. Ma, H. F. & Cui, T. J. Three-dimensional broadband ground-plane cloak made of metamaterials. *Nature Communications* **1**, 21 (2010).
9. Engheta, N., Salandrino, A. & Alu, A. Circuit elements at optical frequencies: Nanoinductors, nanocapacitors, and nanoresistors. *Phys. Rev. Lett.* **95**, 095504 (2005).
10. Zhang, F. *et al.* Negative-Zero-Positive Refractive Index in a Prism-Like Omega-Type Metamaterial. *IEEE Trans. Microwave Theory Tech.* **56**, 2566–2573 (2008).
11. Baena, J., Marques, R., Medina, F. & Martel, J. Artificial magnetic metamaterial design by using spiral resonators. *Phys. Rev. B* **69**, 014402 (2004).
12. Carbonell, J., Torrent, D., Diaz-Rubio, A. & Sanchez-Dehesa, J. Multidisciplinary approach to cylindrical anisotropic metamaterials. *New J. Phys.* **13**, 103034 (2011).
13. Torrent, D. & Sanchez-Dehesa, J. Radial Wave Crystals: Radially Periodic Structures from Anisotropic Metamaterials for Engineering Acoustic or Electromagnetic Waves. *Phys. Rev. Lett.* **103**, 064301 (2009).
14. Torrent, D. & Sanchez-Dehesa, J. Acoustic resonances in two-dimensional radial sonic crystal shells. *New J. Phys.* **12**, 073034 (2010).
15. Kurs, A. *et al.* Wireless power transfer via strongly coupled magnetic resonances. *Science* **317**, 83–86 (2007).
16. Marques, R., Medina, F. & Rafii-El-Idrissi, R. Role of bianisotropy in negative permeability and left-handed metamaterials. *Phys. Rev. B* **65**, 144440 (2002).
17. Pendry, J. B., Holden, A. J., Robbins, D. J. & Stewart, W. J. Magnetism from conductors and enhanced nonlinear phenomena. *IEEE Trans. Microwave Theory Tech.* **47**, 2075–2084 (1999).
18. Pollock, J. G. & Iyer, A. K. Effective-Medium Properties of Cylindrical Transmission-Line Metamaterials. *IEEE Antennas and Wireless Propagation Letters* **10**, 1491–1494 (2011).
19. Comsol, AB (Sweden). Comsol Multiphysics (v. 4.1). (2010).
20. Ansoft. High Frequency Structure Simulator (HFSS), v.14. (2012).
21. Smith, D. R., Vier, D. C., Koschny, T. & Soukoulis, C. M. Electromagnetic parameter retrieval from inhomogeneous metamaterials. *Phys. Rev. E* **71**, 036617 (2005).
22. Yang, Y. *et al.* Optofluidic waveguide as a transformation optics device for lightwave bending and manipulation. *Nature Communications* **3**, 651 (2012).
23. Liu, R. *et al.* Broadband Ground-Plane Cloak. *Science* **323**, 366–369 (2009).
24. Cheng, Q., Cui, T. J., Jiang, W. X. & Cai, B. G. An omnidirectional electromagnetic absorber made of metamaterials. *New J. Phys.* **12**, 063006 (2010).

Acknowledgements

Author contributions

J. C. designed the shells and performed the numerical simulations; M. A. K. and A. P. fabricated the shells; J. C., A. DR. and F. C. designed the measurement setup and A. DR. and F. C. implemented it; A. DR., J. C. and D. T. processed the measurements; J. C., A. P. and J. SD. wrote the manuscript; and J. SD. initiated and supervised the whole project.

Additional information